Far-field model of two-color-laser-driven terahertz radiation including field-element interference and plasma response

Nan Li [1,2] and Wei-Min Wang [1,2,3,*]

[1]*Department of Physics and Beijing Key Laboratory of Opto-electronic Functional Materials and Micro-nano Devices, Renmin University of China, Beijing 100872, China*

[2]*Key Laboratory of Quantum State Construction and Manipulation (Ministry of Education), Renmin University of China, Beijing 100872, China*

[3]*IFSA Collaborative Innovation Center, Shanghai Jiao Tong University, Shanghai 200240, China*

(Received 16 January 2023; accepted 21 September 2023; published 5 October 2023)

The two-color-laser-field scheme for broadband terahertz (THz) radiation from air has been intensively and broadly investigated due to the simplicity of technology and relatively high yield efficiency. Experiments showed that the detected THz angular distribution is usually conical, with a dip in the laser propagation axis which is unfavorable for its application, and the formation of an oscillating tail in the THz waveform has not yet been well understood. Here, we develop an electric-field-element interference model in which each local current source has a phase velocity determined by the laser pulse and a Gaussian temporal profile, rather than an ideal point source, and the current oscillation caused by the plasma dynamics is considered. By introducing the temporal interference, the effects of the phase velocity and the Gaussian profile of the current can correct the THz angular distribution. Therefore, by adjusting the laser pulse duration and the group velocity, the THz angular distribution can be controlled, and the dip can even be eliminated. In addition, the plasma dynamics can result in the formation of an oscillating tail in the THz waveform and sunken spikes in the corresponding spectrum. This is similar to the experimental results, which are usually explained by water-vapor absorption. In turn, the spikes in the spectrum could provide a way to measure the plasma filament density.

DOI: 10.1103/PhysRevA.108.043503

I. INTRODUCTION

Terahertz (THz) waves refer to electromagnetic waves with frequencies in the range of $10^{11}-10^{13}$ Hz, corresponding to a wavelength range of 3 mm–0.03 mm, which is located in the transition region between microwaves and infrared waves. Because of the unique frequency range, THz waves have extensive applications in medical diagnoses, security inspections, and imaging detection [1–9]. Therefore, THz-radiation source generation and THz detection via different approaches have been a hot issue for a long time, and they have seen great progress in recent decades [10–22]. With the development of ultrashort-, ultraintense-laser technology, the ultraintense femtosecond laser pulse has been widely applied for broadband strong THz-radiation generation via the plasma formed from gases [23–28], solids [29,30], and liquids [31–34]. Among them, THz generation from air irradiated by a two-color laser pulse [23–28] has been generally investigated because of its simplicity and stability in experiments and relatively high yields.

The THz mechanism was first attributed to a four-wave mixing process in gas plasma, which can explain partial characteristics of THz radiation such as the THz polarization and the dependence on the relative phase of the two-color laser field [35,36]. Later, Kim *et al.* proposed that the origin of the THz radiation is a net current generated by the symmetry-broken laser-field ionization of gases [37–39] and developed a far-field model successfully explaining the THz conical emission and the intensity dependence [40,41] but could not give the THz waveform and the THz frequency self-consistently. To include the contribution of the plasma dynamics in the THz generation, Wang *et al.* [38,42,43] focused on the evolution of the net current in plasmas and proposed a near-field plasma model, which can obtain the near-single-cycle waveform and the THz central frequency determined by the plasma-oscillation frequency. However, it is hard to verify this model because of the difficulty of measuring the plasma filament density experimentally.

In this article, we combine the two models above together and extend the THz far-field description with the formation of the net current and its evolution in plasmas. In the previous models [40,41], each local current source was considered an ideal point source and emitted THz radiation with the frequency determined by the local plasma density. We consider that each local current source has a phase velocity determined by the group velocity of the laser pulse and the source has a Gaussian temporal profile given by the laser duration and the plasma collision. Then, both the spatial and temporal interference of the emitted THz radiation from each current source can be included. Since the net current has a phase velocity and a temporal profile, we find that the dephasing effect can be influenced by the current duration (or the laser duration) and the laser group velocity, which can be adjusted

*weiminwang1@ruc.edu.cn

by the laser wavelength or the plasma filament density. By decreasing the current or laser duration and the laser group velocity, the conical THz angular distribution with the dip in the laser propagation axis usually observed in experiments can be eliminated.

When the plasma dynamics is considered, an oscillating current appears following the Gaussian current pulse, which can lead to an oscillating tail behind the main THz pulse. The oscillating tail introduces sunken spikes at the corresponding plasma frequencies, which look similar to the absorption peaks. Such a long-time weakly oscillating tail in the THz waveform and sunken spikes in the spectrum were observed in experiments [37,44,45] and are usually interpreted as the absorption of the THz radiation by water vapor. However, the waveform of this oscillating tail is very different from the THz main pulse. The strength of the tail suddenly decreases by one order of magnitude from the main pulse, and the tail maintains an oscillation for a few picoseconds, while the main pulse lasts for only nearly one cycle. Note that the experimental comparison with and without vapor absorption shows [46] the spikes in the THz spectrum are very densely distributed in the frequency range of 1 to 7 THz. However, the THz spectrum observed in two-color-laser experiments [37,44] has several isolated spikes. These features cannot be completely explained by the absorption of water vapor but could be attributed to the evolution of the dynamic current in the plasma in our model. Furthermore, the oscillating tail and the corresponding spikes in the spectrum could provide a way to measure the plasma filament density. Each spike in the spectrum corresponds to a plasma frequency $\omega_{\text{spike}} = \frac{1}{\sqrt{2}}\omega_p = \frac{1}{\sqrt{2}}\sqrt{\frac{n_{e0}e^2}{m\epsilon_0}}$, which is connected to the plasma density n_{e0}. Thus, one can read the plasma-density information in the spectrum from these spikes.

II. MODEL AND SIMULATION RESULTS

A. The far-field model with a Gaussian profile of the plasma current

In the two-color-field scheme, the THz radiation is generated from a dynamic current like other electromagnetic emission in classical electrodynamics [47]. This current originates from a gas-ionization process and then follows the physics of the current evolution in plasmas. The photoionization current model [37] shows that the symmetry-broken electric field generates a net current which leads to the THz radiation. We will start our investigation with this idea and extend the spatial interference of the point sources (spherical wave) to the temporal interference of current sources with a Gaussian temporal profile. Then, the angular distribution and the frequency spectrum of the THz radiation can be self-consistently calculated, rather than assuming monochromatic radiation [40]. In addition, we consider a current source with a phase velocity equal to the laser group velocity to correct the spatial and temporal interference results. Finally, the plasma oscillation is also considered, which can explain the oscillating tail of the THz radiation observed in experiments.

We consider a gas molecule at the position $\vec{x}'$. When a two-color laser pulse passes through it, the molecule is ionized at time t', and an electron is born with an initial velocity of zero. In the laser field, it gains the velocity

$$v(t) = -\frac{e}{m_e}\int_{t'}^{t} E_L(\tau)d\tau, \tag{1}$$

where e and m_e are the electron charge and mass, respectively. A two-color laser electric field can be written as

$$E_L(r,t) = E_\omega f_1 e^{-\frac{t^2}{\tau_1^2}}\cos(\omega t) + E_{2\omega} f_2 e^{-\frac{t^2}{\tau_2^2}}\cos(\omega t + \theta), \tag{2}$$

where $f_1(r)$ and $f_2(r)$ are transverse profiles of the fundamental wave laser field and its second harmonic, respectively, τ_1 and τ_2 are pulse durations, and θ is the relative phase between the fundamental wave and its second harmonic. We consider the laser spot size and the duration to be far greater than the laser wavelength and the period, so its transverse and longitudinal distributions can be ignored. Then, the laser field can be simplified as

$$E_L(t) = E_\omega\cos(\omega t) + E_{2\omega}\cos(\omega t + \theta). \tag{3}$$

The electron velocity can be expressed as

$$v(t) = -\frac{eE_\omega}{m_e\omega}\sin(\omega t) - \frac{eE_{2\omega}}{2m_e\omega}\sin(\omega t + \theta) + v_d(t'), \tag{4}$$

where

$$v_d(t') = \frac{eE_\omega}{m_e\omega}\sin(\omega t') + \frac{eE_{2\omega}}{2m_e\omega}\sin(\omega t' + \theta). \tag{5}$$

Equations (4) and (5) show that the generated electron has an oscillation velocity and a drift velocity $v_d(t')$, where the drift velocity is determined by the laser-field strength and the relative phase at the ionization position. Assuming that the electron density is $dN_e(t')$, we obtain a current $dN_e(t')v(t)$. Note that the current or the velocity oscillating at the laser frequency does not generate THz-band radiation [48] and what really contributes is the drift current $dN_e(t')v_d(t')$. With a suitable relative phase θ, a stronger laser field causes a higher ionization probability, a larger drift velocity, and, eventually, a stronger net current. It should be noted that the relative phase between the fundamental wave and its second harmonic changes periodically during the propagation because they have different phase velocities. The dephasing length L_{dp} can be defined as

$$L_{\text{dp}} = \frac{\lambda_{2\omega}}{n_{2\omega} - n_\omega}, \tag{6}$$

where n_ω and $n_{2\omega}$ are refractive indices for the fundamental wave and its second harmonic, respectively, and $\lambda_{2\omega}$ is the wavelength of the second harmonic.

With the two-color laser pulse passing through a local position, the current is continuously accumulated, as shown in Fig. 1(a). For a Gaussian laser pulse, at the time point t_1, the current accumulation speed (slope of the blue line) is slow due to the low laser intensity; at the time point t_2, the laser intensity reaches the peak, and the current increases the fastest. At the time point t_3, when the laser is about to leave, the current increases slowly again and reaches a peak value. The rising edge of the current from t_1 to t_3 has a timescale approaching the laser duration. Then, the current is attenuated by the collision [49] of the plasma composed of electrons and nearly immobile ions. Hence, the typical lifetime of the

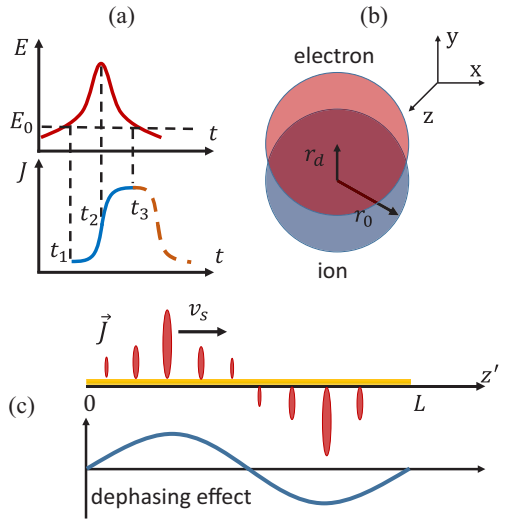

FIG. 1. (a) The Gaussian laser pulse (top) and the corresponding current (bottom), where E_0 is the ionization threshold and t_1, t_2, and t_3 are three different times. (b) The charge oscillation caused by the separation of the electron and the ion density center in the laser polarization direction (y direction), where r_d is the deviation of the electron center from the ion center, r_0 is the plasma filament radius, and $r_0 \gg r_d$. (c) The dynamic current (top), including the dephasing effect (bottom), where v_s is the phase velocity of the current, L is the plasma filament length, and $\vec{J}$ is a temporal profile of the current at a given z'. During the propagation, the current magnitude and the polarity change along with z' because of the dephasing effect

current is several hundred femtoseconds, which is determined by the duration of the laser pulse plus the characteristic time of the plasma collision [49]. The plasma collision determines the current falling edge with a timescale of tens or hundreds of femtoseconds. For simplicity, we take a Gaussian time profile of the current with the falling edge equal to the rising edge since the timescale of the two edges is the same order.

As the laser pulse propagates forward, new net currents are continuously excited at new positions. Actually, the net current does not move with the laser pulse since the electron velocity is transverse, and therefore, the formed currents have a phase velocity v_s equal to the laser group velocity. The formed currents only oscillate transversely at local positions, as displayed in Fig. 1(b). These currents, which form at different positions, follow a similar evolution process, but the overall magnitudes and polarities are different because of the dephasing effect, as shown in Fig. 1(c). The dynamic transverse current can emit THz radiation with vector potential $\vec{A}$ in the far field:

$$\vec{A}(\vec{x},t) = \frac{\mu_0}{4\pi}\int dV' \frac{\vec{J}\left(\vec{x}', t-\frac{r}{c}\right)}{r}; \tag{7}$$

we can further obtain the THz electric field $\vec{E}$,

$$\vec{E}(\vec{x},t) = -\frac{\partial \vec{A}(\vec{x},t)}{\partial t}, \tag{8}$$

and the THz angular distribution,

$$I(\Theta) = \int_{-\infty}^{\infty} |E(\Theta,t)|^2 dt. \tag{9}$$

We consider the current to have a temporal profile of a Gaussian with a duration of τ, i.e.,

$$\vec{J}(\vec{x}',t) = \vec{J}_0 \cos\left(\frac{2\pi}{L_{\rm dp}}z' + \phi_0\right)\tau^{\frac{1}{2}} e^{-(\frac{t-\frac{z'}{v_s}}{\tau})^2}, \tag{10}$$

where the cosine term represents the modulation of the current due to the dephasing effect, $L_{\rm dp}$ is the dephasing length which comes from the phase velocity difference between the fundamental wave and its second harmonic, ϕ_0 is the initial relative phase at the beginning edge of the plasma filament, and τ is the current duration.

In our model (also in [40,41]), the field ionization is not included, and the net current via the ionization is taken directly. For the two-color scheme, the THz radiation is generated from the net current, and this current is a specific result of the symmetry-broken two-color laser field. The relative phase between the fundamental wave and its second harmonic changes with the propagation of the two-color laser. This relative phase determines the magnitude and the polarity of the current. If a single-color laser is used, the symmetry of the laser-field ionization cannot be broken, and a net current is not generated. Therefore, our model cannot be applied in the single-color scheme [49,50].

Next, we analyze the mechanism of the dephasing effect on the THz angular distribution. As the laser pulse propagates forward, the plasma filament and currents are formed. For instance, when the pulse passes through positions A, B, and C marked in Fig. 2(a), the THz radiation sources are emitted with electric-field elements E_S^A, E_S^B, and E_S^C, respectively. These electric-field elements propagate to the far-field point O and superpose temporally to form a THz pulse. We assume that the plasma filament is composed of $N(N \to \infty)$ slices with thickness L/N, where L is the length of the plasma filament. Then, each slice contains a current pulse emitting an electric-field element. The final THz pulse at the far-field point O is the coherent superposition of N electric-field elements. For a Gaussian current with a characteristic duration τ, as shown in Fig. 2(b), a generated electric-field element can be expressed as

$$E_s^i(t) = (\pm 1)_i A_s^i \frac{2(t-t_i)}{\tau^{\frac{3}{2}}} e^{-(\frac{t-t_i}{\tau})^2}, \tag{11}$$

where $E_s^i(t)$ indicates this contribution comes from the ith slice, $(\pm 1)_i$ represents the polarity of the electric-field element, A_s^i is the amplitude of this field element when it arrives at the far-field point O, and t_i is the time delay. Then the THz intensity is given by

$$I \propto \sum_{i<j}^{N}\sum_{j=1}^{N}\left[\int_{-\infty}^{\infty} 2E_s^i(t)E_s^j(t)dt\right] + \sum_{i=1}^{N}\int_{-\infty}^{\infty}\left[E_s^i(t)\right]^2 dt. \tag{12}$$

For further analysis, we give its integral result:

$$I \propto \sum_{i<j}^{N}\sum_{j=1}^{N}(\pm 1)_i(\pm 1)_j 2A_s^i A_s^j e^{-\frac{1}{2}(\frac{t_i-t_j}{\tau})^2}\left[1-\left(\frac{t_i-t_j}{\tau}\right)^2\right] + \sum_{i=1}^{N} A_s^{i\,2}. \tag{13}$$

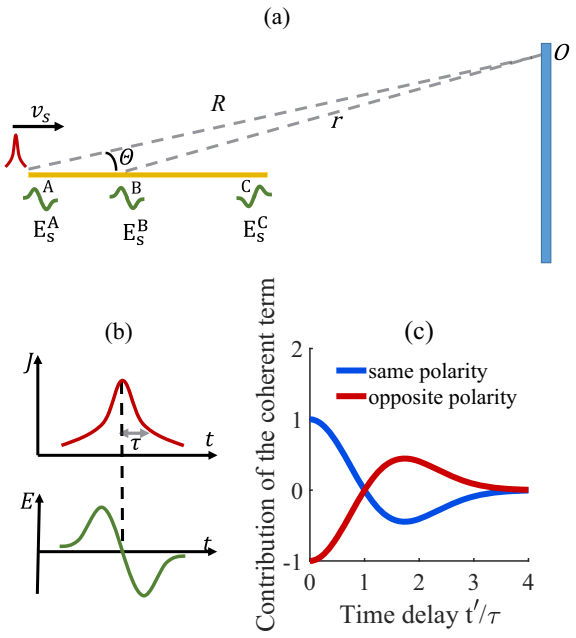

FIG. 2. Schematic diagram of the electric-field-element interference model. (a) E_S^A, E_S^B, and E_S^C are electric-field elements excited by the currents at three positions, A, B, and C, where A is the beginning point of the filament and C is the ending point, R is the distance from A to the far-field point O, and Θ is the included angle between OA and the filament. (b) An electric-field element emitted from a Gaussian current with a characteristic duration of τ at a given position. (c) The contribution of a coherent term [in Eq. (12)] of two electric-field elements to the THz intensity, where the time delay between the two elements is t'. Note that positive and negative values denote positive and negative contributions to the THz intensity observed at the far-field point O.

The first term in Eq. (12) is the coherent superposition of $N(N-1)/2$ pairs of electric-field elements, and the second term is a constant. When the laser pulse reaches slice A at time 0, the corresponding electric-field element at point O starts to appear at time R/c. When the laser pulse moves to slice B at time t, the corresponding electric-field element at point O starts to appear at time $R/c + (1 - \frac{v_s}{c}\cos\Theta)t$. Considering the interference of two electric-field elements with a time delay t', we have

$$t' = \left(1 - \frac{v_s}{c}\cos\Theta\right)\frac{\Delta L}{v_s}, \tag{14}$$

where ΔL is the distance between the two slices. As illustrated in Fig. 2(c), with $t' = 0$, the coherent term will make a positive contribution to the total THz intensity if the two elements have the same polarity (blue line). Otherwise, the coherent term will make a negative contribution and weaken the total THz intensity (red line). While $t' > 4\tau$, the two elements are almost separated temporally, and the coherent term makes no contribution to the total THz intensity.

The ratio t'/τ reflects the dephasing effect and strongly influences the THz angular distribution. For example, we take typical parameters to be $v_s = 0.9997c$ (the group velocity of the 800-nm laser in air), filament length $L = 30$ mm, and current duration $\tau = 0.15$ ps. When the observation point is at 0°, the time delay t' between A and C is 0.03 ps, far less than τ. When the observation point is at 5°, t' rises to 0.41 ps, close to 3τ. Therefore, the observed THz angular distribution can be affected much more strongly at $\Theta = 0°$ than $\Theta = 5°$ due to the dephasing effect. If there is no dephasing effect and all electric-field elements have the same polarity, all coherent terms make positive contributions and lead to a THz intensity peak appearing at 0° since t' is much smaller than τ. For an angle of 5° with $t' \approx 3\tau$, this large time delay causes the coherent terms to make nearly no contributions to the THz intensity, which causes the intensity to be weaker than that at 0°. Therefore, the THz angular distribution is a single peak without the dephasing effect considered, as shown in [40]. However, with the dephasing effect, the angular distribution will transition from a single peak to double peaks. This is because any coherent pair with opposite polarity will decrease the THz intensity at small angles. For example, in typical conditions, the numbers of positive and negative currents are equal; the numbers of coherent pairs with the same polarity and with opposite polarity are $\frac{N}{2}(\frac{N}{2}-1)$ and $\frac{N}{2}\frac{N}{2}$, respectively, and the latter is $\frac{N}{2}$ more than the former. For 0°, the value t'/τ is close to zero for almost all coherent pairs; therefore, the $\frac{N}{2}$ net negative contributions make the THz intensity decrease at this angle. These negative contributions can finally make the THz intensity at 0° much smaller than at other medium angles. This will be illustrated by our simulation in Figs. 3 and 4.

B. Control of the THz angular distribution by reducing the dephasing effect

In the previous model, when the plasma filament length is long enough, the impact of the dephasing effect is hard to weaken with changing the THz angular distribution. This is because the concept of point sources [40] ignores the fact that the THz radiation emitted from each source has a broad spectrum and the role of the group velocity v_g of the two-color laser pulse is not considered, which indicates the THz angular distribution given in the previous models [40] needs to be updated. In our model, we extend the spatial interference of ideal point sources (a spherical wave) to the temporal interference of dynamic current sources with a Gaussian temporal profile, determined by the laser pulse duration and the plasma collision, which can show the frequency spectrum of the local radiation emitting from each source. We take the current phase velocity v_s as the group velocity of the two-color laser pulse, which can significantly modulate the interference results. With the updated interference and broad spectra of the radiation sources, we can obtain a more self-consistent THz angular distribution and waveforms. Meanwhile, our model also provides a way to control the THz angular distribution by adjusting the laser pulse duration and the group velocity to weaken the impact of the dephasing effect.

For fixed filament length L, dephasing length $L_{\rm dp}$, and initial relative phase ϕ_0, by changing the current duration τ and the phase velocity v_s,we obtain the new angular distribution of the THz intensity. Starting from a typical double-peak distribution result with τ_0 and v_{s0}, an arbitrary coherent term contribution can be described by $\eta = \frac{t'}{\tau} = (1 - \frac{v_{s0}}{c}\cos\Theta_0)\frac{\Delta L}{v_{s0}\tau_0}$ according to Eq. (14). When the laser group

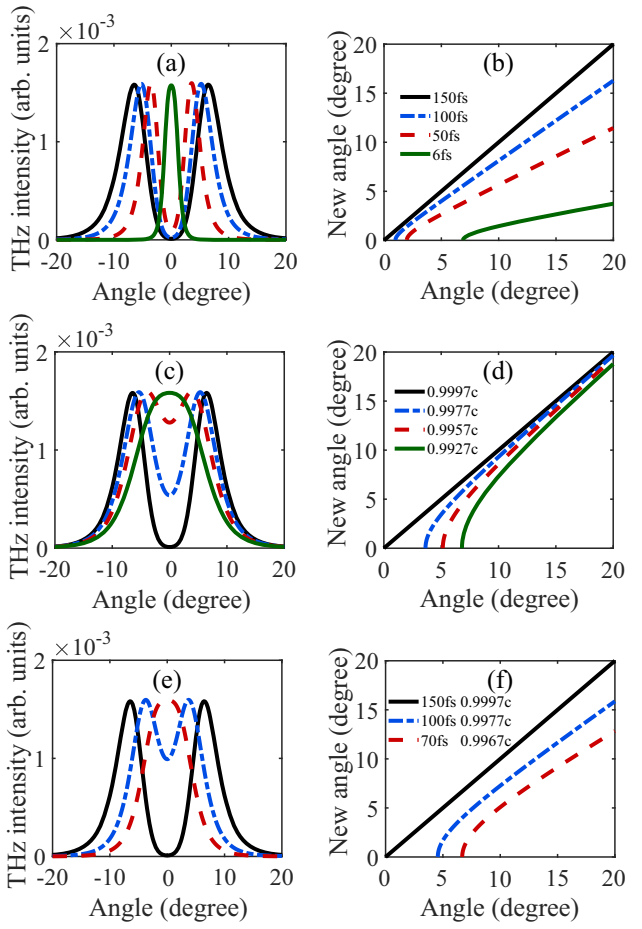

FIG. 3. THz angular distributions with (a) different current pulse durations τ, (c) different laser group velocities v_s, and (e) different τ and v_s. (b), (d), and (f) The new angle as a function of the original angle when we change the typical parameters ($v_s = 0.9997c$, $\tau = 150$ fs) to another set of parameters corresponding to (a), (c), and (e), respectively. Here, the initial laser relative phase $\phi_0 = 0.5\pi$ and filament length $L = L_{\rm dp} = 20$ mm are used in all panels, $v_s = 0.9997c$ is fixed in (a) and (b), and $\tau = 150$ fs is fixed in (c) and (d).

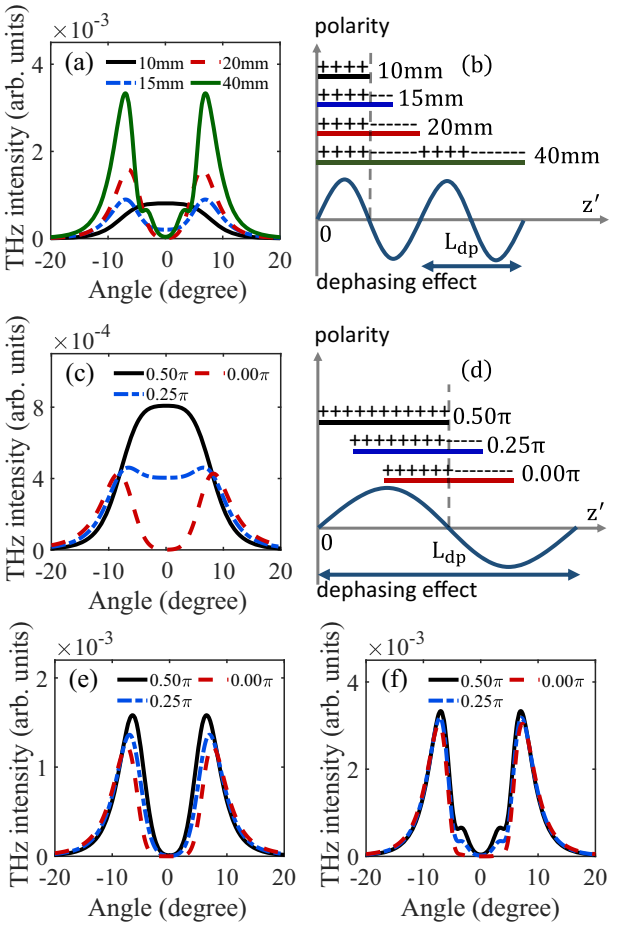

FIG. 4. THz angular distributions for different plasma filament lengths and initial phases. (a) Comparison of the angular distribution for different filament lengths L of 5, 10, 20, and 40 mm, where $\phi_0 = 0.50\pi$. (b) A possible interpretation of the dephasing effect. (c) Comparison of the angular distribution for different initial phases ϕ_0 of 0.50π, 0.25π, and 0, where $L = 10$ mm. (d) A possible interpretation of the dephasing effect. THz angular distributions for different initial phases of 0.50π, 0.25π, and 0, where we take the filament lengths (e) $L = 20$ mm and (f) $L = 40$ mm. Here, we take $L_{\rm dp} = 20$ mm and $\tau = 150$ fs.

velocity v_{s0} is lowered to v_{s1} or the dynamic current duration τ_0 is decreased to τ_1 so that

$$\eta = \left(1 - \frac{v_{s0}}{c}\cos\Theta_0\right)\frac{\Delta L}{v_{s0}\tau_0} = \left(1 - \frac{v_{s1}}{c}\cos\Theta_1\right)\frac{\Delta L}{v_{s1}\tau_1}, \tag{15}$$

the THz intensity value at Θ_0 shifts towards a smaller angle Θ_1; that is, double peaks of the angular distribution could shift towards 0°. These phenomena are displayed in Fig. 3. Note that the current duration τ can be determined by the laser duration, and the laser group velocity v_s can be adjusted by the gas density and the laser wavelength.

Figure 3(a) shows the change in the THz angular distribution when the current pulse duration is varied. When the current duration is 150 fs (close to the laser duration), the angular distribution has double peaks away from 0°, as is usually observed in experiments [25]. As the current duration is decreased to 100 and 50 fs, the distance between the double peaks is reduced. With a further decrease in the duration to a very small value of 6 fs, the angular distribution transitions to a single peak at 0°. In Fig. 3(c) we decrease the laser group velocity from $v_s = 0.9997c$ and find that the THz intensity near 0° is significantly improved. The dip at 0° is completely filled with $v_s = 0.9927c$, and the angular distribution also transitions to a single peak.

Notice that the evolution of the angular distribution in Figs. 3(a) and 3(c) shows different behaviors. With the decrease of the duration τ, the width of double peaks is reduced, and the peaks shift towards 0°. While the velocity v_s decreases, the width is broadened. This can be understood through Figs. 3(b) and 3(d), in which the angle displacement of the THz intensity can be defined as the difference between the original angle and the new angle. When the duration τ is decreased, the angle displacement is large for a large original angle, causing the peak width to be reduced. While

the velocity v_s is decreased, the angle displacement is large for a small original angle, giving rise to a broadened peak width. Combined parameter configurations are displayed in Figs. 3(e) and 3(f); they show that the control of the angular distribution can be realized under a more relaxed condition by using both two methods together.

The relationship among the filament length, the dephasing length, and the initial relative phase of the two-color laser field also plays an important role in the angular distribution of THz intensity and the THz yield. For example, the change in the THz yield shows a different dependence on the gas pressure in different focus situations [51,52]. For the long-focus condition [51], the filament length is longer than or comparable to the dephasing length, and increasing the dephasing length by reducing the gas pressure is helpful for improving the THz yield. However, for the short-focus condition [52], the filament length is much shorter than the dephasing length. Increasing the gas pressure will decrease the dephasing length, but the filament length is too short to be influenced by the dephasing length change. In this case a higher gas pressure causes higher electron density, which can result in a higher THz yield. Another example will be shown below in which the dephasing effect can be sufficiently decreased and even avoided by adjusting the initial relative phase for a short filament (e.g., below $L_{\rm dp}$), but for a long filament this method does not work since the dephasing effect acts periodically.

We change the filament length and the initial relative phase of the two-color laser field, and the THz angular distribution is shown in Fig. 4. In Fig. 4(a), as the filament length is increased from 10 to 40 mm, the THz angular distribution transits from a single-peak pattern to a double-peak pattern, and the overall THz intensity is enhanced. This result can be explained by Fig. 4(b). Here, we take $L_{\rm dp} = 20$ mm, and therefore, the polarity of electric-field elements for the first 10 mm is positive, and it is negative in the following 10 mm. When $L = 10$ mm, all electric-field elements have positive polarity, so the THz intensity has a single peak at 0°. When $L = 15$ mm, the extra part of 5 mm has negative polarity, which makes the THz intensity decrease at 0°, and a small dip appears at this angle. When $L = 20$ and 40 mm, the amount of positive and negative polarity is equal, the dephasing effect at 0° is enhanced, and the dip becomes deeper. In addition, the number of electric-field elements is proportional to the filament length, which causes the overall THz intensity to be enhanced with the increase of the filament length.

In Fig. 4(c), when changing the initial relative phase from 0.50π to 0.25π and 0 (note that the overall THz intensity is very low in this case [53]), we find that the THz angular distribution changes from a single-peak pattern to a double-peak one. Note that we take $L = 10$ mm in Fig. 4(c). The result can be explained by Fig. 4(d). For a given filament length, the polarity of electric-field elements can also be changed by adjusting the initial phase. When $\phi_0 = 0.50\pi$, all electric-field elements have positive polarity, so the THz intensity has a single peak at 0°. When $\phi_0 = 0.25\pi$, a quarter of the electric-field elements have negative polarity, which makes the THz intensity decline at 0°, and a dip appears. When $\phi_0 = 0$, half of the electric-field elements have negative polarity, the dephasing effect at 0° is enhanced, and the dip becomes deeper. In Figs. 4(e) and 4(f) we increase the filament length to 20 and 40 mm, respectively, and find that the angular distribution of double peaks always appears at any initial phase. All these results suggest that the dephasing effect can influence the THz angular distribution destructively but can be eliminated by adjusting various parameters.

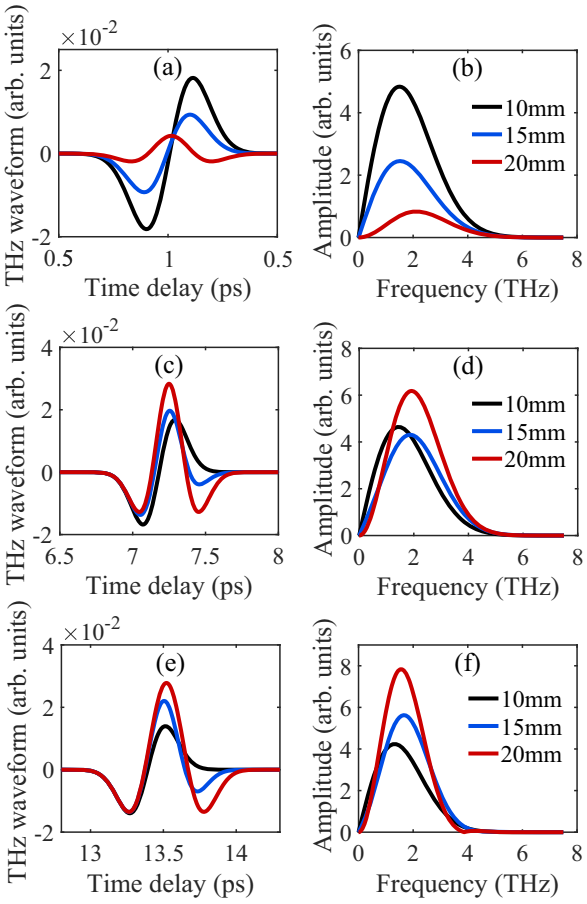

FIG. 5. Left column: THz waveforms observed at different angles, (a) 1°, (c) 5°, and (e) 7°. Right column: the corresponding spectra, (b) 1°, (d) 5°, and (f) 7°. In each plot, different curves correspond to filament lengths of 10, 15, and 20 mm. Here, $\tau = 150$ fs, $v_s = 0.9997c$, $L_{\rm dp} = 20$ mm, and $\phi_0 = 0.50\pi$ are taken.

C. THz waveforms from different-length filaments

In addition to the angular distribution, the dephasing effect can also influence the THz waveform and the spectrum, as shown in Fig. 5. In Fig. 5 we plot THz waveforms and spectra generated from plasma filaments with different lengths observed at different angles. In Fig. 5(a) the THz pulses are observed at 1°. When the filament length is increased from 10 to 20 mm (equal with $L_{\rm dp}$), the waveform remains nearly a single cycle but changes from one kind of waveform observed in experiments [37,44] to another type observed in other experiments [23,36]. Meanwhile, the THz field strength is decreased due to the dephasing effect. When the observation angle is shifted to 5° and 7° [see Figs. 5(c) and 5(e)], the waveforms are similar to the corresponding ones at 1°, but the overall strengths for $L = 15$ mm and $L = 20$ mm are increased, which is consistent with the angular distribution of THz intensity of

double peaks. We can also see that there are obvious time delays between different THz waveforms at different angles since the THz signals are collected at a distance of 500 mm away from the filament and a larger angle causes a longer distance and a longer time delay. In addition, a slight shift of the peak frequency is observed in the THz spectra [Figs. 5(b), 5(d), and 5(f)] with the increase of the filament length, in agreement with the waveform change caused by the dephasing effect.

D. Formation of the THz oscillating tail due to the plasma oscillation

As described by Eqs. ((7)–(9), the THz radiation characteristics are mainly determined by the current form $\vec{J}(\vec{x}', t)$. In the previous section, we adopted a Gaussian current profile as shown in Eq. (10) to contain the finite current duration which can lead to the single-cycle THz waveform. In this section, we take the current form to be a Gaussian current profile plus an oscillating tail to describe the plasma-oscillation effect. Accompanied by current production due to gas ionization, a plasma also forms. After the passage of the two-color laser pulse, the electrons gain transverse velocities, while the ions are nearly immobile because they have a much higher mass than electrons. Then, the electrons or currents oscillate transversely around the immobile ions, and a periodically varying charge separation is formed with a plasma-oscillation frequency. The amplitude of the current oscillation gradually decreases with the electron collision and the energy loss of THz emission; thus, we take the current form to be a Gaussian current profile (the current produced via the ionization) plus an oscillating tail (due to the plasma oscillation).

We consider the charge separation to be a small deviation of the electron center from the ion center [54], as illustrated in Fig. 1(b). The transverse electric field generated by the ion distribution is $E_R^i = \frac{Zen_{i0}}{2\epsilon_0}R$ at $(-r_0 \leqslant R \leqslant r_0)$, and the electric field generated by the electron distribution is $E_R^e = -\frac{en_{e0}}{2\epsilon_0}(R - r_d)$ at $(-r_0 + r_d \leqslant R \leqslant r_0 + r_d)$ under a small displacement r_d from the ion center, where ϵ_0 is the dielectric constant, n_{i0} is the ion density, and n_{e0} is the electron density. The total electric field is $E = \frac{en_{e0}}{2\epsilon_0}r_d$, generated by the charge separation with a displacement r_d between the ion and the electron center. Inserting this field into the electron-motion equation, we can solve the oscillation frequency of the electrons or the current:

$$\omega_{\rm osc} = \frac{1}{\sqrt{2}}\sqrt{\frac{n_{e0}e^2}{m\epsilon_0}} = \frac{1}{\sqrt{2}}\omega_p. \tag{16}$$

This plasma dynamics causes the current to oscillate with a frequency of $\omega_{\rm osc}$. Thus, the THz pulse also has a frequency component of $\omega_{\rm osc}$.

In Fig. 6(a), we take three different currents: one has a Gaussian profile, and the other two have a Gaussian profile plus an oscillating tail caused by the plasma oscillation with plasma frequencies of 2 and 4 THz; the generated THz pulses are shown by the gray dot-dashed, blue solid, and red solid lines, respectively. Comparing these three THz-pulse waveforms, we can see the plasma oscillation in the current causes a small-amplitude oscillating tail in the THz pulse at

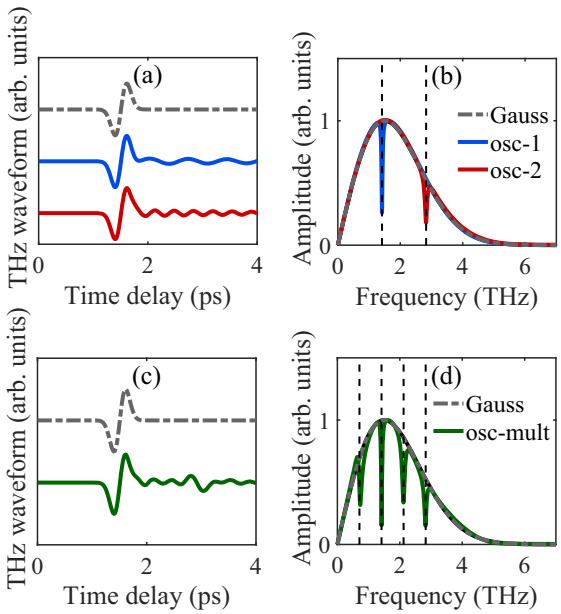

FIG. 6. THz waveforms calculated at 1° and spectra generated by plasma currents with different forms. (a) waveforms generated by plasma currents with a Gaussian profile (gray dot-dashed line) and a Gaussian pulse plus an oscillating tail with plasma frequencies of 2 THz (blue solid line) and 4 THz (red solid line). (b) Spectra corresponding to (a). (c) waveforms generated by plasma currents with a Gaussian profile (gray dot-dashed line) and a Gaussian pulse plus an oscillating tail containing plasma frequency components of 1, 2, 3, and 4 THz (green solid line). (d) Spectra corresponding to (c). In (b) we plot two vertical lines at $\frac{2}{\sqrt{2}}$ and $\frac{4}{\sqrt{2}}$ THz, and in (d) we plot four vertical lines at $\frac{1}{\sqrt{2}}$, $\frac{2}{\sqrt{2}}$, $\frac{3}{\sqrt{2}}$, and $\frac{4}{\sqrt{2}}$ THz.

a frequency according to Eq. (16). With the plasma oscillation, these THz waveforms are similar to the typical results observed in experiments [37,45], which have a large amplitude near a single-cycle waveform lasting for hundreds of femtoseconds and a following weak oscillating tail lasting for several picoseconds. The former can be attributed to the contribution of the Gaussian current, and the latter can be attributed to the plasma oscillation.

The corresponding spectra are plotted in Fig. 6(b), which shows that the plasma oscillation results in sunken spikes around $2/\sqrt{2}$ and $4/\sqrt{2}$ THz. With the plasma oscillation, the sunken spikes formed in the spectrum are similar to that observed in experiments [37,44,55]. Usually, the oscillating tail in the THz waveform and the corresponding spikes in the spectrum are considered to be caused by the water-vapor absorption. It should be pointed out that the experimental comparison with and without vapor absorption shows [46] the spikes in the THz spectrum are very densely distributed in the frequency range of 1 to 7 THz. However, the THz spectra observed from two-color-laser experiments [37,44] have several isolated spikes. Obviously, the plasma-oscillation effect could explain such isolated sunken spikes and the corresponding oscillating tail in the THz waveform, as shown in Figs. 6(a) and 6(b). Each isolated spike corresponds to an efficient plasma-density component since a filament basically has a nonuniform plasma-density profile, which can cause a

THz pulse with a few efficient plasma frequencies, as shown in Figs. 6(c) and 6(d). In turn, the spikes in the spectrum could reflect the main plasma-density components in the filament. In fact, the plasma-oscillation effect can result in not only sunken spikes but also protuberant peaks at corresponding frequencies in the THz spectrum, which is influenced by the time delay between the main Gaussian current and the following oscillating current tail.

In our model, we have adopted a source current form with a Gaussian shape to describe its finite duration. This duration consists of two parts: its rising edge comes from the ionization process of the two-color laser pulses, and its falling edge comes from the collision process [49]. These two parts can be asymmetric in duration, but it reflects the fact that the net current should have a lifetime. In the limit of the lifetime approaching zero, the source current form reduces to the δ function, which brings an infinitely wide spectrum of the THz radiation emitted from any source. Note that the oscillation frequency $\omega_p/\sqrt{2}$ comes from the condition of an infinitely long cylinder with uniform density [56,57]. Because the longitudinal length of the plasma filament is much larger than its transverse size, it is reasonable to make the assumption of infinite filament length. For a cylinder plasma with finite dimensions and an inhomogeneous density profile, we can assume that this plasma has a uniform density at its average density for simplicity. Obviously, this approximation is better than an infinite-plasma assumption, which gives the oscillation at the plasma frequency ω_p.

III. CONCLUSION

We developed a far-field model to calculate the angular distribution, the waveform, and the spectrum of THz radiation generated via the two-color-laser scheme. We considered each field element to originate from a local current source in the plasma filament and the current source to have a phase velocity determined by the laser group velocity and a Gaussian temporal profile given by the laser pulse duration and the plasma collision. As a result, the spatial interference of ideal point sources in the previous model is extended to the temporal and spatial interference of dynamic current sources. In this way, the current oscillation caused by the plasma dynamics can be included in our model. The plasma dynamics can result in an oscillating tail in the THz waveform and sunken spikes in the corresponding spectrum, similar to the experimental observation that is usually explained by water-vapor absorption. Apart from presenting another possible explanation for the observed oscillating tail, the corresponding spikes in the spectrum could also provide an approach for measuring the plasma filament density. With the current-source phase velocity and the temporal profile considered, the laser group velocity and the duration can affect the dephasing effect. Decreasing the laser pulse duration and the group velocity can improve the angular distribution of the THz intensity and can even eliminate the dip around 0° usually observed in experiments. Adjusting the filament length and the initial relative phase of the two-color laser pulse could vary the angular distribution and the waveform of the THz radiation.

ACKNOWLEDGMENTS

This work was supported by the Strategic Priority Research Program of the Chinese Academy of Sciences (Grant No. XDA25050300), the National Key R&D Program of China (Grant No. 2018YFA0404801), the Fundamental Research Funds for the Central Universities, Research Funds of Renmin University of China (Grant No. 20XNLG01) and Computational resources have been provided by the Physical Laboratory of High Performance Computing at Renmin University of China.

[1] E. Pickwell and V. Wallace, J. Phys. D **39**, R301 (2006).
[2] Y. Shen, A. T. Lo, P. Taday, B. Cole, W. Tribe, and M. Kemp, Appl. Phys. Lett. **86**, 241116 (2005).
[3] P. Gaal, K. Reimann, M. Woerner, T. Elsaesser, R. Hey, and K. H. Ploog, Phys. Rev. Lett. **96**, 187402 (2006).
[4] Z. Jiang and X.-C. Zhang, Opt. Lett. **23**, 1114 (1998).
[5] A. Dobroiu, C. Otani, and K. Kawase, Meas. Sci. Technol. **17**, R161 (2006).
[6] M. Tonouchi, Nat. Photonics **1**, 97 (2007).
[7] X. C. Zhang, A. Shkurinov, and Y. Zhang, Nat. Photonics **11**, 16 (2017).
[8] K. Moldosanov, A. Postnikov, V. Lelevkin, and N. Kairyev, Ferroelectrics **509**, 158 (2017).
[9] M. Massaouti, C. Daskalaki, A. Gorodetsky, A. D. Koulouklidis, and S. Tzortzakis, Appl. Spectrosc. **67**, 1264 (2013).
[10] D. H. Auston, K. P. Cheung, J. A. Valdmanis, and D. A. Kleinman, Phys. Rev. Lett. **53**, 1555 (1984).
[11] M. Bass, P. Franken, J. Ward, and G. Weinreich, Phys. Rev. Lett. **9**, 446 (1962).
[12] A. Nahata, A. S. Weling, and T. F. Heinz, Appl. Phys. Lett. **69**, 2321 (1996).
[13] G. Scalari, C. Walther, J. Faist, H. Beere, and D. Ritchie, Appl. Phys. Lett. **88**, 141102 (2006).
[14] H. Ito, F. Nakajima, T. Furuta, and T. Ishibashi, Semicond. Sci. Technol. **20**, S191 (2005).
[15] G. Gallot and D. Grischkowsky, J. Opt. Soc. Am. B **16**, 1204 (1999).
[16] M. Tani, K.-S. Lee, and X.-C. Zhang, Appl. Phys. Lett. **77**, 1396 (2000).
[17] A. D. Koulouklidis, C. Gollner, V. Shumakova, V. Y. Fedorov, A. Pugžlys, A. Baltuška, and S. Tzortzakis, Nat. Commun. **11**, 292 (2020).
[18] T. Oh, Y. Yoo, Y. You, and K. Kim, Appl. Phys. Lett. **105**, 041103 (2014).
[19] L. A. Johnson, J. P. Palastro, T. M. Antonsen, and K.-Y. Kim, Phys. Rev. A **88**, 063804 (2013).
[20] D. Kuk, Y. Yoo, E. Rosenthal, N. Jhajj, H. Milchberg, and K. Kim, in *CLEO: QELS_Fundamental Science* (Optical Society of America, Washington, DC, 2016), p. FTh3M–5
[21] K. Kim and Y. You, Nat. Photonics **8**, 92 (2014).
[22] T. Oh, Y. You, N. Jhajj, E. Rosenthal, H. Milchberg, and K. Kim, New J. Phys. **15**, 075002 (2013).
[23] D. Cook and R. Hochstrasser, Opt. Lett. **25**, 1210 (2000).

[24] T. Bartel, P. Gaal, K. Reimann, M. Woerner, and T. Elsaesser, Opt. Lett. **30**, 2805 (2005).
[25] H. Zhong, N. Karpowicz, and X.-C. Zhang, Appl. Phys. Lett. **88**, 261103 (2006).
[26] K.-Y. Kim, A. Taylor, J. Glownia, and G. Rodriguez, Nat. Photonics **2**, 605 (2008).
[27] D. Kuk, Y. Yoo, E. Rosenthal, N. Jhajj, H. Milchberg, and K.-Y. Kim, Appl. Phys. Lett. **108**, 121106 (2016).
[28] I. Babushkin, W. Kuehn, C. Kohler, S. Skupin, L. Berge, K. Reimann, M. Woerner, J. Herrmann, and T. Elsaesser, Phys. Rev. Lett. **105**, 053903 (2010).
[29] G.-Q. Liao, Y.-T. Li, Y.-H. Zhang, H. Liu, X.-L. Ge, S. Yang, W.-Q. Wei, X.-H. Yuan, Y.-Q. Deng, B.-J. Zhu, Z. Zhang, W.-M. Wang, Z.-M. Sheng, L.-M. Chen, X. Lu, J.-L. Ma, X. Wang, and J. Zhang, Phys. Rev. Lett. **116**, 205003 (2016).
[30] G.-Q. Liao, Y.-T. Li, H. Liu, G. G. Scott, D. Neely, Y.-H. Zhang, B.-J. Zhu, Z. Zhang, C. Armstrong, E. Zemaityte, P. Bradford, P. G. Huggard, D. R. Rusby, P. McKenna, C. M. Brenner, N. C. Woolsey, W.-M. Wang, Z.-M. Sheng, and J. Zhang, Proc. Natl. Acad. Sci. USA **116**, 3994 (2019).
[31] I. Dey, K. Jana, V. Y. Fedorov, A. D. Koulouklidis, A. Mondal, M. Shaikh, D. Sarkar, A. D. Lad, S. Tzortzakis, A. Couairon, and G. R Kumar, Nat. Commun. **8**, 1184 (2017).
[32] Q. Jin, J. Dai, Y. E, and X.-C. Zhang, Appl. Phys. Lett. **113**, 261101 (2018).
[33] L.-L. Zhang, W.-M. Wang, T. Wu, S.-J. Feng, K. Kang, C.-L. Zhang, Y. Zhang, Y.-T. Li, Z.-M. Sheng, and X.-C. Zhang, Phys. Rev. Appl. **12**, 014005 (2019).
[34] Y. Chen, Y. He, L. Liu, Z. Tian, and J. Dai, Opt. Lett. **47**, 5969 (2022).
[35] M. Kress, T. Löffler, S. Eden, M. Thomson, and H. G. Roskos, Opt. Lett. **29**, 1120 (2004).
[36] X. Xie, J. Dai, and X.-C. Zhang, Phys. Rev. Lett. **96**, 075005 (2006).
[37] K.-Y. Kim, J. H. Glownia, A. J. Taylor, and G. Rodriguez, Opt. Express **15**, 4577 (2007).
[38] W.-M. Wang, Z.-M. Sheng, H.-C. Wu, M. Chen, C. Li, J. Zhang, and K. Mima, Opt. Express **16**, 16999 (2008).
[39] K.-Y. Kim, Phys. Plasmas **16**, 056706 (2009).
[40] Y. S. You, T. I. Oh, and K. Y. Kim, Phys. Rev. Lett. **109**, 183902 (2012).
[41] A. Gorodetsky, A. D. Koulouklidis, M. Massaouti, and S. Tzortzakis, Phys. Rev. A **89**, 033838 (2014).
[42] W.-M. Wang, S. Kawata, Z.-M. Sheng, Y.-T. Li, and J. Zhang, Phys. Plasmas **18**, 073108 (2011).
[43] W.-M. Wang, P. Gibbon, Z.-M. Sheng, and Y.-T. Li, Phys. Rev. Lett. **114**, 253901 (2015).
[44] K. Liu, A. D. Koulouklidis, D. G. Papazoglou, S. Tzortzakis, and X.-C. Zhang, Optica **3**, 605 (2016).
[45] Y. Tan, H. Zhao, W.-M. Wang, R. Zhang, Y.-J. Zhao, C.-L. Zhang, X.-C. Zhang, and L.-L. Zhang, Phys. Rev. Lett. **128**, 093902 (2022).
[46] J. Liu, J. Dai, S. L. Chin, and X.-C. Zhang, Nat. Photonics **4**, 627 (2010).
[47] J. D. Jackson, *Classical Electrodynamics*, 3rd ed. (Wiley, New York, 2001).
[48] H. Roskos, M. Thomson, M. Kreß, and T. Löffler, Laser Photonics Rev. **1**, 349 (2007).
[49] P. Sprangle, J. R. Penano, B. Hafizi, and C. A. Kapetanakos, Phys. Rev. E **69**, 066415 (2004).
[50] C. D'Amico, A. Houard, M. Franco, B. Prade, A. Mysyrowicz, A. Couairon, and V. T. Tikhonchuk, Phys. Rev. Lett. **98**, 235002 (2007).
[51] Y.-J. Yoo, D. Jang, and K.-Y. Kim, Opt. Express **27**, 22663 (2019).
[52] G. Rodriguez and G. L. Dakovski, Opt. Express **18**, 15130 (2010).
[53] W.-M. Wang, Y.-T. Li, Z.-M. Sheng, X. Lu, and J. Zhang, Phys. Rev. E **87**, 033108 (2013).
[54] Z. Zhang, Y. Chen, M. Chen, Z. Zhang, J. Yu, Z. Sheng, and J. Zhang, Phys. Rev. Lett. **117**, 243901 (2016).
[55] K. Liu, D. Papazoglou, A. Koulouklidis, S. Tzortzakis, and X.-C. Zhang, in *2015 40th International Conference on Infrared, Millimeter, and Terahertz Waves (IRMMW-THz)* (IEEE, Piscataway, NJ, 2015), pp. 1–2.
[56] C. S. Liu and V. K. Tripathi, J. Appl. Phys. **105**, 013313 (2009).
[57] A. Bystrov, N. V. Vvedenskii, and V. B. Gildenburg, J. Exp. Theor. Phys. Lett. **82**, 753 (2005).